



Article

Switching Neural Network Control for Underactuated Spacecraft Formation Reconfiguration in Elliptic Orbits

Jinlong Yu D, Zhi Li *, Lu Jia D and Yasheng Zhang

Department of Aerospace Science and Technology, Space Engineering University, Beijing 101416, China; yunudt@126.com (J.Y.); 18510793099@163.com (L.J.); zhangyspublic@163.com (Y.Z.)

* Correspondence: lizhipublic@163.com

Abstract: A switching neural network control scheme, consisting of the adaptive neural network controller and sliding mode controller, is proposed for underactuated formation reconfiguration in elliptic orbits with the loss of either the radial or in-track thrust. By using the inherent coupling of system states, the switching neural network technique is then adopted to estimate the unmatched disturbances and design the underactuated controller to achieve underactuated formation reconfiguration with high precision. The adaptive neural network controller works in the active region, and the disturbances composed of linearization errors and external perturbations are approximated by radial basis function neural networks. The adaptive sliding mode controller works outside the active region, and the upper bound of the approximation errors is estimated by the adaptation law. The stability of the closed-loop control system is proved via the Lyapunov-based approach. The numerical simulation results have demonstrated the rapid, high-precision and robust performance of the proposed controller compared with the linear sliding mode controller.

Keywords: spacecraft formation; formation reconfiguration; underactuated spacecraft; switching neural network



Citation: Yu, J.; Li, Z.; Jia, L.; Zhang, Y. Switching Neural Network Control for Underactuated Spacecraft Formation Reconfiguration in Elliptic Orbits. *Appl. Sci.* 2022, 12, 5792. https://doi.org/10.3390/ app12125792

Academic Editors: Shengping Gong, Wen Yao and Xu Huang

Received: 20 May 2022 Accepted: 5 June 2022 Published: 7 June 2022

Publisher's Note: MDPI stays neutral with regard to jurisdictional claims in published maps and institutional affiliations.



Copyright: © 2022 by the authors. Licensee MDPI, Basel, Switzerland. This article is an open access article distributed under the terms and conditions of the Creative Commons Attribution (CC BY) license (https://creativecommons.org/licenses/by/4.0/).

1. Introduction

Spacecraft formation flight is rapidly becoming a hot topic of research in space with its great potential for Earth observation, in-orbit services, deep space imaging and exploration [1–3]. It decentralizes the functions of a single spacecraft into a group of smaller ones, thereby reducing risk and cost and improving reliability and adaptability [4]. The ability of these spacecrafts to reshape or retarget from one formation to another completes the formation reconfiguration, greatly increasing the flexibility of formation missions. The methods of formation reconfiguration using continuous thrust can generally be divided into two categories: fully actuated and underactuated. Fully actuated means that there are independent control channels in the radial, in-track and normal directions. The current research on consensus with formation reconfiguration focuses on fully-actuated systems, a series of control methods have been proposed for the full-actuated formation reconfiguration mission such as sliding mode control, state Riccati equations, adaptive control, and neural network control [5–7]. If the thrusters break down in one direction, the number of independent controls of the system is less than the degrees of freedom, it becomes an underactuated system, which cannot complete the reconfiguration mission, and the above control schemes are then not applicable anymore. Although the installation of backup thrusters can solve this problem, considering the need for light weight and miniaturization of spacecraft in the future, it is more economical and effective to design an underactuated control scheme.

Focusing on the fully actuated reconfiguration problems, scholars at home and abroad have conducted much research, but seldom have works that deal with the underactuated reconfiguration been reported in the literature. Leonard et al. examined the feasibility of

formation control using only in-track differential atmospheric drag [8] and a linear feedback controller for underactuated formation reconfiguration was designed by Kumar et al. [9]. Godard et al. designed a nonlinear controller for formation reconfiguration without in-track thrust [10]. Yin et al. designed an impulsive control strategy for the elliptical relative motion based on the relative orbit elements [11]. Huang et al. derived the optimal analytical solution for an underactuated formation reconfiguration in circular orbits and proposed an underactuated controller for formation reconfiguration in elliptical orbits [12,13]. Yasuhiro proposed the control scheme to achieve the optimal formation reconfiguration with bounded and small attitude changes using only a few thrusters [14]. The traditional formation reconfiguration control adopts the linearized CW equations [15] or Tschauner-Hempel equations [16] to model the relative motion of the satellites within the formation and ignores the external perturbation [17,18]. To overcome this requirement, neural networks are capable of approximating arbitrary smooth functions on tight sets with arbitrary accuracy and are therefore widely used to estimate nonlinear uncertainties in system dynamics. Despite the ability to approximate with high accuracy, approximation errors still exist. As a result, in most previous work [19–21], it was only possible to guarantee that the state error was consistently and eventually bounded, or that it was arbitrarily small if the feedback gain [22] was sufficiently large. Neural network-based controllers need to add more nodes when the application range increases in order to meet the higher accuracy, which leads to a complex structure and too much computation for real-time in-orbit calculations. Inaccurate estimation of the neural network will also affect the performance of the whole controller and even cause the system to diverge. To address such issues, Xia et al. [23] designed a spacecraft rendezvous and docking controller based on a coupled orbit-attitude dynamic model by combining adaptive methods with the backstepping method using switching functions. With similar methods, Sun et al. [24] proposed a neural networks controller for spacecraft formation using only aerodynamic forces. Given that linearization errors and external disturbances do exist in the dynamics of underactuated formation reconfiguration in elliptic orbits, a switching neural network controller (SNNC) for the underactuated spacecraft formation reconfiguration problem is proposed, using adaptive neural network controllers to approximate the uncertainties in the neural active region and using adaptive sliding mode controllers to approximate uncertainties outside the active region. The proposed SNNC enhances the steady-state control accuracy and does not rely on the upper bound of the uncertainties, thus, could improve the robustness of the system against uncertainties. Compared with the existing related research, the main contributions of this article can be summarized as follows.

- 1. The nonlinear terms and perturbations in the dynamics model of underactuated SFF are estimated in real-time by a neural network to obtain higher control accuracy.
- 2. The adaptation laws of the radial-based neural networks derived by using Lyapunov's method are provided to estimate the unknown parameters of the system so that it is not necessary to know the upper bound of the perturbation in advance.
- The control scheme is able to complete the underactuated formation reconfiguration
 task in elliptic orbits with the loss of radial or in-track thrust, improving the reliability
 of the task completion.

The paper is structured as follows: Section 2 develops a model for the dynamics of underactuated spacecraft formations in elliptical orbits; Section 3 details the closed-loop state feedback controller design method, and numerical simulations are given in Section 4 to verify the performance of the proposed controllers. Finally, Section 5 concludes the full text.

2. Dynamic Model of Underactuated SFF

Consider the chief spacecraft in the formation flying in elliptical orbits. As depicted in Figure 1, two reference frames are used to describe the relative motion between the chief and deputy, $O_E X_I Y_I Z_I$ is the Earth-centered inertial (ECI) frame with O_E being the center of Earth, and $O_C xyz$ is the local-vertical local-horizontal (LVLH) frame fixed at the center

Appl. Sci. 2022, 12, 5792 3 of 16

of the chief O_C , where the x axis is pointing in the radial direction of the chief, the z axis is normal to the orbital plane, and the y axis completes the right-handed frame.

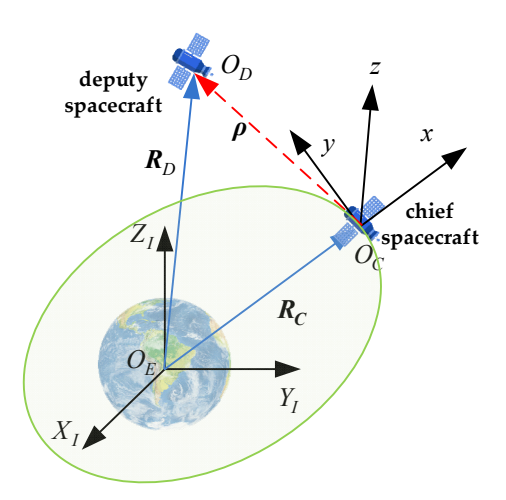


Figure 1. Definition of coordinate frames.

Therefore, the orbital equations of underactuated SFF can be written in the state space form as [10].

$$\dot{X} = AX + m_d^{-1}(B_iU_i + DF), \ i = 1, 2,$$
 (1)

with

$$\mathbf{A} = \begin{bmatrix}
0 & 0 & 0 & 1 & 0 & 0 \\
0 & 0 & 0 & 0 & 1 & 0 \\
0 & 0 & 0 & 0 & 0 & 1 & 0 \\
\omega_{C}^{2} + 2n_{C}^{2} & \alpha_{C} & 0 & 0 & 2\omega_{C} & 0 \\
-\alpha_{C} & \omega_{C}^{2} - n_{C}^{2} & 0 & -2\omega_{C} & 0 & 0 \\
0 & 0 & -n_{C}^{2} & 0 & 0 & 0
\end{bmatrix}, \mathbf{B}_{i} = \begin{bmatrix}\mathbf{0}_{3\times2} \\ \mathbf{B}_{i2}\end{bmatrix},$$

$$\mathbf{B}_{12} = \begin{bmatrix}
0 & 0 \\
1 & 0 \\
0 & 1
\end{bmatrix}, \mathbf{B}_{22} = \begin{bmatrix}
1 & 0 \\
0 & 0 \\
0 & 1
\end{bmatrix}, \mathbf{D} = \begin{bmatrix}
0 & 0 & 0 \\
0 & 0 & 0 \\
0 & 0 & 0 \\
1 & 0 & 0 \\
0 & 0 & 1
\end{bmatrix}.$$
(2)

Denote the relative state vector of the deputy as $\mathbf{X} = \begin{bmatrix} \rho^{\mathrm{T}} & \dot{\rho}^{\mathrm{T}} \end{bmatrix}^{\mathrm{T}}$, where $\boldsymbol{\rho} = \begin{bmatrix} x & y & z \end{bmatrix}^{\mathrm{T}}$ and $\dot{\boldsymbol{\rho}} = \begin{bmatrix} \dot{x} & \dot{y} & \dot{z} \end{bmatrix}^{\mathrm{T}}$ are the relative position vector and relative velocity vector, respectively, $\omega_C = n_C \sqrt{(1+e\cos\theta)}$ is the angular velocity of the chief and $\alpha_C = -2n_C^2e\sin\theta$ is the angular acceleration of the chief, $n_C = \sqrt{\mu/R_C^3}$, μ is the Earth's gravitational constant, R_C is the radius of the deputy e and θ are, respectively, the eccentricity and true anomaly, m_D is the mass of the deputy spacecraft, $F \in \mathbb{R}^3 = \begin{bmatrix} d_x & d_y & d_z \end{bmatrix}^{\mathrm{T}}$ denotes the vector of total disturbances including the nonlinear terms and perturbations. For the case without radial control, the control input is denoted as $\mathbf{U}_1 = \begin{bmatrix} U_y & U_z \end{bmatrix}^{\mathrm{T}}$. For the case without in-track control, the control input is denoted as $\mathbf{U}_2 = \begin{bmatrix} U_x & U_z \end{bmatrix}^{\mathrm{T}}$.

The controllability of the underactuated systems and the feasibility of reconfiguration have been well investigated in the literature [13] and lead to the following lemma:

Appl. Sci. 2022, 12, 5792 4 of 16

Lemma 1. For the case without radial control, formation reconfiguration in elliptical orbit is still feasible without any supplementary conditions. For the case without in-track control, it is conditionally feasible provided that the condition $\widetilde{x}_{\rm I}(0) = \widetilde{x}_{\rm II}(0)$ holds, where $\widetilde{x}_{\rm I}(0)$ and $\widetilde{x}_{\rm II}(0)$ are the coordinate transformations of the relative radial positions of the chief and deputy spacecraft in configuration I and configuration II respectively at the initial moment, and can be expressed as:

$$\begin{cases} \widetilde{x}_{I}(0) = (1 + e\cos\theta)x_{I}(0), \\ \widetilde{x}_{II}(0) = (1 + e\cos\theta)x_{II}(0). \end{cases}$$
 (3)

Since the uncontrollable state of the system $\tilde{x}_{\rm I}(0)=(1+e_{\rm C}\cos\theta_{\rm C})x_{\rm I}(0)$ keeps its initial value constant during the reconfiguration process, the preconditions for achieving configuration II are naturally satisfied when the above conditions are met, so the reconfiguration is still feasible in the case of in-track underactuated.

3. Controller Design

3.1. RBFNN

The radial basis function neural network (RBFNN) has been extensively used in control system design because it can approximate any continuous nonlinear function with a compact set and arbitrary accuracy [24,25], and can adapt and learn the dynamic properties of uncertain systems. For a continuous nonlinear function $f(X) \in \mathbb{R}^n$, a RBFNN can approximate it on a compact as:

$$f(X) = W^{*T}h(X) + \varepsilon, \tag{4}$$

where X is the input vector, ε is the approximation error of the unknown upper bound, W^* is the ideal weight value of the network output, and $h = [h_1 \ h_2 \dots h_n]^T$ is the radial basis function vector denoted as:

$$h_j(\mathbf{X}) = \exp\left(-\|\mathbf{X} - C_j\|^2/(2b_j^2)\right), \ j = 1, 2, \dots, n.$$
 (5)

where $h_j(X)$ is the output of the jth neuron in the hidden layer, C_j and b_j is the center and width of the Gaussian basis function of the jth neuron, and n is the number of nodes of the neural network.

3.2. Controller for the Case without Radial Control

Define the desired relative state of motion as $X_d = \begin{bmatrix} \boldsymbol{\rho}_d^{\mathrm{T}} & \dot{\boldsymbol{\rho}}_d^{\mathrm{T}} \end{bmatrix}^{\mathrm{T}}$, where $\boldsymbol{\rho}_d = \begin{bmatrix} x_d & y_d & z_d \end{bmatrix}^{\mathrm{T}}$ and $\dot{\boldsymbol{\rho}}_d = \begin{bmatrix} \dot{x}_d & \dot{y}_d & \dot{z}_d \end{bmatrix}^{\mathrm{T}}$ are the desired relative position vector and relative velocity vector, respectively, and the desired dynamics equation for the elliptical orbital underactuated formation can be formulated as follows:

$$\dot{X}_{id} = AX_{id}, i = 1, 2.$$
 (6)

The error dynamics system obtained by making the difference between Equations (1) and (6) is given by:

$$\dot{e}_i = Ae_i + m^{-1}(B_iU_i + D_i), i = 1, 2.$$
 (7)

where $e_i = X_i - X_{id}$ is the error state vector. Then the error dynamics equation in the absence of radial control can be rewritten as [13].

$$\begin{cases}
\dot{e}_{1u} = A_{11}e_{1u} + A_{12}e_{1a} + m^{-1}d_{1u}, \\
\dot{e}_{1a} = A_{13}e_{1u} + A_{14}e_{1a} + m^{-1}(U_1 + d_{1a}),
\end{cases} (8)$$

Appl. Sci. 2022, 12, 5792 5 of 16

with

$$A_{11} = \begin{bmatrix} 0 & 0 & 0 & 1 \\ 0 & 0 & 0 & 0 \\ 0 & 0 & 0 & 0 \\ \omega_{C}^{2} + 2n_{C}^{2} & \alpha_{C} & 0 & 0 \end{bmatrix}, \quad A_{12} = \begin{bmatrix} 0 & 0 \\ 1 & 0 \\ 0 & 1 \\ 2\omega_{C} & 0 \end{bmatrix},$$

$$A_{13} = \begin{bmatrix} -\alpha_{C} & \omega_{C}^{2} - n_{C}^{2} & 0 & -2\omega_{C} \\ 0 & 0 & -n_{C}^{2} & 0 \end{bmatrix}, \quad A_{14} = \begin{bmatrix} 0 & 0 \\ 0 & 0 \end{bmatrix}.$$

$$(9)$$

where $e_{1u} = \begin{bmatrix} e_x & e_y & e_z & \dot{e}_x \end{bmatrix}^T$, $e_{1a} = \begin{bmatrix} \dot{e}_y & \dot{e}_z \end{bmatrix}^T$, $d_{1u} = \begin{bmatrix} \mathbf{0}_{1\times 3} & d_y \end{bmatrix}^T$ and $d_{1a} = \begin{bmatrix} d_y & d_z \end{bmatrix}^T$. Note that $e_{1u} \in \mathbb{R}^4$ and $e_{1a} \in \mathbb{R}^2$, we make a linear transformation of e_{1u} to obtain a new variable $\bar{e}_{1u} = C_{11}e_{1u} \in \mathbb{R}^2$, where $C_{11} \in \mathbb{R}^{2\times 4}$ is the design parameter matrix denoting the linear transformation for e_{1u} from four dimensions to two dimensions,

$$C_{11} = \begin{bmatrix} k_{11} & k_{12} & 0 & k_{13} \\ 0 & 0 & 1 & 0 \end{bmatrix} \tag{10}$$

where k_{11} , k_{12} and k_{13} are the controller design parameters. Then the dynamics of \bar{e}_{1u} is given by:

$$\dot{\bar{e}}_{1u} = (C_{12} + \dot{C}_{11})e_{1u} + C_{13}e_{1a} + m^{-1}C_{11}d_{1u}$$
(11)

with

$$C_{12} = C_{11}A_{11}, \quad C_{13} = C_{11}A_{12} = \begin{bmatrix} k_{12} + 2\omega_C k_{13} & 0\\ 0 & 1 \end{bmatrix}.$$
 (12)

The sliding surface is then chosen as:

$$s_1 = [s_{11} \quad s_{12}]^{\mathrm{T}} = \alpha_1 \overline{e}_{1u} + [(C_{12} + \dot{C}_{11})e_{1u} + C_{13}e_{1a}] \approx \alpha_1 \overline{e}_{1u} + \dot{\overline{e}}_{1u}, \tag{13}$$

where $\alpha_1 > 0$ is a positive constant, the control law is designed as:

$$U_1 = u_{1eq} + u_{1s}, (14)$$

where u_{1eq} is the equivalent control and u_{1s} is the reaching law, respectively designed as:

$$u_{1eq} = -\hat{m}\overline{A}_1 - \delta_1, u_{1s} = \dot{s}_1 = -\hat{m}C_{13}^{-1}[K_1s_1 + \eta_1 \operatorname{sig}^{\sigma_1}(s_1)],$$
(15)

with

$$\overline{A}_{1} = C_{13}^{-1} \left[(\dot{C}_{12} + \ddot{C}_{11}) e_{1u} + \dot{C}_{13} e_{1a} + (C_{12} + \dot{C}_{11}) (A_{11} e_{1u} + A_{12} e_{1a}) + C_{13} e_{1a} \right]
+ (A_{13} e_{1u} + A_{14} e_{1a}) + \alpha_{1} C_{13}^{-1} \left[(C_{12} + \dot{C}_{11}) e_{1u} + C_{13} e_{1a} \right],
\delta_{1} = C_{13}^{-1} \left[(C_{12} + \dot{C}_{11}) d_{1u} \right] + d_{1a} + \alpha_{1} C_{13}^{-1} C_{11} d_{1u},
\operatorname{sig}^{\sigma_{1}}(s_{1}) = \left[|s_{11}|^{\sigma_{1}} \operatorname{sgn}(s_{11}) |s_{12}|^{\sigma_{1}} \operatorname{sgn}(s_{12}) \right]^{\mathsf{T}},$$
(16)

where \hat{m} is the estimated value of the mass, and δ_1 is the total disturbance. The total disturbance δ_1 can be approximated by RBFNN in the active region. Substituting Equation (4) into Equation (14) yields.

$$U_1 = -\hat{m}\overline{A}_1 - W_1^{*T}h(X) - \varepsilon_1 + u_{1s}, \tag{17}$$

where $X = \begin{bmatrix} x y z \dot{x} \dot{y} \dot{z} \end{bmatrix}^T$ is the input vector. Although the RBFNN has the ability to approximate the disturbance with high accuracy, the approximation error still exists. In order to reduce the approximation error, the upper bound of the error needs to be updated and estimated by the adaptive law. Defining ϕ_i as the upper bound of the estimation error

Appl. Sci. 2022, 12, 5792 6 of 16

 ε_i , denote $\hat{\phi}_i = [\hat{\phi}_{i1}, \hat{\phi}_{i2}]^T$ as the estimate of ϕ_i , and \hat{W}_1 as the estimate of the neural network weights, Equation (17) can be rewritten as:

$$\mathbf{U}_{1} = -\hat{m}\overline{A}_{1} - \hat{\mathbf{W}}_{1}^{T}\mathbf{h}(\mathbf{X}) - \operatorname{diag}(\hat{\phi}_{11}, \hat{\phi}_{12})\operatorname{sgn}(\mathbf{s}_{1}) + \mathbf{u}_{1s}. \tag{18}$$

The adaptive sliding mode control method is used to automatically adjust the control gain to compensate for the uncertainty in the upper bound outside the active region, and the control law is designed as:

$$\mathbf{U}_1 = -\hat{m}\overline{A}_1 - \hat{\delta}_1 + \mathbf{u}_{1s},\tag{19}$$

where $\hat{\delta}_1$ is an estimate of the unknown upper bound of perturbations. A nonlinear function $\hbar_{a,b}(e_{\rho})$ is chosen to construct the switching function [26].

$$\hbar_{a,b}(\mathbf{e}_i) = \begin{cases}
0, & \|\mathbf{e}_i\| \le a, \\
1 - \cos^2\left(\frac{\pi}{2}\sin^2\left(\frac{\pi}{2}\frac{\|\mathbf{e}_i\|^2 - a^2}{b^2 - a^2}\right)\right), & a < \|\mathbf{e}_i\| < b, \\
1, & \|\mathbf{e}_i\| \ge b,
\end{cases}$$
(20)

where 0 < a < b are design parameters to determine the neural active region. The input to the switching function is the error state e_i . The switching control law combining the neural network control law and the adaptive sliding mode control law is designed as:

$$U_1 = -\hat{m}\overline{A}_1 + (1 - \hbar_{a,b}(e_\rho))u_{n1} + \hbar_{a,b}(e_\rho)u_{s1} + u_{1s}, \tag{21}$$

with

$$u_{n1} = -\hat{W}_1^T h(X) - \text{diag}(\hat{\phi}_{11}, \hat{\phi}_{12}) \text{sgn}(s_1),$$

 $u_{s1} = -\hat{\delta}_1.$ (22)

The adaptive laws of \hat{m} , \hat{W}_1 , $\hat{\phi}_1$ and $\hat{\delta}_1$ in Equation (21) are designed as:

$$\begin{cases}
\hat{m} = \gamma_1 \mathbf{s}_1^{\mathsf{T}} \overline{\mathbf{A}}_1, \\
\dot{\mathbf{W}}_1 = (1 - \hbar_{a,b} e_{\rho})) \boldsymbol{\xi}_1 \boldsymbol{h}(\mathbf{X}) \mathbf{s}_1^{\mathsf{T}}, \\
\dot{\hat{\boldsymbol{\phi}}}_1 = (1 - \hbar_{a,b}(e_{\rho})) \boldsymbol{\xi}_2 |\mathbf{s}_1|, \\
\dot{\hat{\delta}}_1 = \hbar_{a,b}(e_{\rho}) \boldsymbol{\xi}_3 \mathbf{s}_1,
\end{cases} (23)$$

where $\gamma_1 > 0$, ξ_1 , ξ_2 and ξ_3 are diagonal positive definite matrices. To demonstrate the stability of the closed-loop control system, consider the Lyapunov candidate function.

$$V_1 = (1/2)(\boldsymbol{s}_1^{\mathsf{T}} \boldsymbol{m} \boldsymbol{s}_1 + \gamma_1^{-1} \widetilde{\boldsymbol{m}}^2 + \operatorname{tr}(\widetilde{\boldsymbol{W}}_1^{\mathsf{T}} \boldsymbol{\xi}_1 \widetilde{\boldsymbol{W}}_1) + \widetilde{\boldsymbol{\phi}}_1^{\mathsf{T}} \boldsymbol{\xi}_2^{-1} \widetilde{\boldsymbol{\phi}}_1 + \widetilde{\boldsymbol{\delta}}_1^{\mathsf{T}} \boldsymbol{\xi}_3^{-1} \widetilde{\boldsymbol{\delta}}_1)$$
(24)

where $\tilde{m} = \hat{m} - m$, $\tilde{W}_1 = \hat{W}_1 - {W_1}^*$, $\tilde{\phi}_1 = \hat{\phi}_1 - \phi_1$ and $\tilde{\delta}_1 = \hat{\delta}_1 - \delta_1$ are the estimation errors of m, W_1^* , ϕ_1 and δ_1 , respectively. Taking the time derivative of Equation (24) and substituting Equation (23) into the derivative of Equation (24) yields.

Appl. Sci. 2022, 12, 5792 7 of 16

$$\dot{V}_{1} = s_{1}^{\mathsf{T}} m \dot{s}_{1} + \gamma_{1}^{-1} \widetilde{m} \dot{m} + tr(\widetilde{W}_{1}^{\mathsf{T}} \xi_{1} \dot{W}_{1}) + \widetilde{\boldsymbol{\phi}}_{1}^{\mathsf{T}} \xi_{2}^{-1} \dot{\hat{\boldsymbol{\phi}}}_{1} + \widetilde{\delta}_{1}^{\mathsf{T}} \xi_{3}^{-1} \dot{\hat{\boldsymbol{\delta}}}_{1}
= s_{1}^{\mathsf{T}} m(\overline{A}_{1} + m^{-1}(\boldsymbol{U}_{1} + \delta_{1})) + \gamma_{1}^{-1} \widetilde{m} \dot{m} + tr(\widetilde{W}_{1}^{\mathsf{T}} \xi_{1} \dot{W}_{1}) + \widetilde{\boldsymbol{\phi}}_{1}^{\mathsf{T}} \xi_{2}^{-1} \dot{\hat{\boldsymbol{\phi}}}^{1} + \widetilde{\delta}_{1}^{\mathsf{T}} \xi_{3}^{-1} \dot{\hat{\boldsymbol{\delta}}}_{1}
= -s_{1}^{\mathsf{T}} (K_{1} s_{1} + \boldsymbol{\eta}_{1} sig^{\sigma_{1}}(s_{1})) + s_{1}^{\mathsf{T}} \delta_{1} - s_{1}^{\mathsf{T}} \hat{\boldsymbol{\delta}}_{1} + tr(\widetilde{W}_{1}^{\mathsf{T}} \xi_{1} \dot{W}_{1}) + \widetilde{\boldsymbol{\phi}}_{1}^{\mathsf{T}} \xi_{2}^{-1} \dot{\hat{\boldsymbol{\phi}}}_{1} + \widetilde{\delta}_{1}^{\mathsf{T}} \xi_{3}^{-1} \dot{\hat{\boldsymbol{\delta}}}_{1}
= -s_{1}^{\mathsf{T}} (K_{1} s_{1} + \boldsymbol{\eta}_{1} sig^{\sigma_{1}}(s_{1})) + s_{1}^{\mathsf{T}} (1 - \hbar)(-\widetilde{W}_{1} h(x) + \varepsilon_{1} - diag(\widehat{\boldsymbol{\phi}}_{1}) sgn(s_{1})) + (1 - \hbar)\left(s_{1}^{\mathsf{T}} \widetilde{\boldsymbol{W}}_{1} h(x) + \widetilde{\boldsymbol{\phi}}_{1} | s_{1}|\right)
= -s_{1}^{\mathsf{T}} (K_{1} s_{1} + \boldsymbol{\eta}_{1} sig^{\sigma_{1}}(s_{1})) + (1 - \hbar)(s_{1}^{\mathsf{T}} \varepsilon_{1} - \boldsymbol{\phi}_{1} | s_{1}|)
= -(1 - \hbar) \sum_{i=1}^{2} |s_{1i}| (\boldsymbol{\phi}_{1i} - \varepsilon_{1i} sgn(s_{1i})) - s_{1}^{\mathsf{T}} K_{1} s_{1} - s_{1}^{\mathsf{T}} \boldsymbol{\eta}_{1} sig^{\sigma_{1}}(s_{1})
\leq -(1 - \hbar) \sum_{i=1}^{2} |s_{1i}| (\boldsymbol{\phi}_{1i} - \varepsilon_{1i} sgn(s_{1i})) - K_{11} ||s_{1}||^{2} - \eta_{11} ||s_{1}||^{\sigma_{1}+1} < 0.$$

Therefore, the underactuated closed-loop system is asymptotically stable.

3.3. Controller for the Case without In-Track Control

Similar to the approach in the case without radial control, for the case without in-track control, the error dynamics system can be rewritten as:

$$\begin{cases}
\dot{e}_{2u} = A_{21}e_{2u} + A_{22}e_{2a} + m^{-1}d_{2u}, \\
\dot{e}_{2a} = A_{23}e_{2u} + A_{24}e_{2a} + m^{-1}(U_2 + d_{2a}),
\end{cases} (26)$$

with

$$A_{21} = \begin{bmatrix} 0 & 0 & 0 & 0 & 0 \\ 0 & 0 & 0 & 1 & 1 \\ 0 & 0 & 0 & 0 & 0 \\ -\alpha_{C} & \omega_{C}^{2} - n_{C}^{2} & 0 & 0 \end{bmatrix}, \quad A_{22} = \begin{bmatrix} 1 & 0 \\ 0 & 0 \\ 0 & 1 \\ -2\omega_{C} & 0 \end{bmatrix},$$

$$A_{23} = \begin{bmatrix} \omega_{C}^{2} + 2n_{C}^{2} & \alpha_{C} & 0 & 2\omega_{C} \\ 0 & 0 & -n_{C}^{2} & 0 \end{bmatrix}, \quad A_{24} = \begin{bmatrix} 0 & 0 \\ 0 & 0 \end{bmatrix},$$

$$(27)$$

where $e_{2u} = \begin{bmatrix} e_x & e_y & e_z & \dot{e}_y \end{bmatrix}^T$, $e_{2a} = \begin{bmatrix} \dot{e}_x & \dot{e}_z \end{bmatrix}^T$, $d_{2u} = \begin{bmatrix} \mathbf{0}_{1\times3} & d_y \end{bmatrix}^T$ and $d_{2a} = \begin{bmatrix} d_x & d_z \end{bmatrix}^T$. The control input is $\mathbf{U}_2 = \begin{bmatrix} U_x & U_z \end{bmatrix}^T$.

Similarly, note that $e_{2u} \in \mathbb{R}^4$ and $e_{2a} \in \mathbb{R}^2$, a linear transformation $\overline{e}_{2u} = C_{21}e_{2u} \in \mathbb{R}^2$ is performed, and the matrix C_{21} is given by,

$$C_{21} = \begin{bmatrix} 0 & k_{21} & 0 & k_{22} \\ 0 & 0 & 1 & 0 \end{bmatrix}. \tag{28}$$

The dynamic equations of \bar{e}_{2u} can be expressed as:

$$\dot{\overline{e}}_{2u} = (\dot{C}_{21} + C_{22})e_{2u} + C_{23}e_{2a} + m^{-1}C_{21}d_{2u}, \tag{29}$$

with

$$C_{22} = C_{21}A_{21}, \quad C_{23} = C_{21}A_{22} = \begin{bmatrix} -2\omega_C k_{22} & 0\\ 0 & 1 \end{bmatrix}.$$
 (30)

The sliding surface is then chosen as:

$$s_{2} = \left[s_{21} \quad s_{22}\right]^{\mathrm{T}} = \alpha_{2}\bar{e}_{2u} + \left[\left(P_{22} + \dot{P}_{21}\right)e_{2u} + P_{23}e_{2a}\right] \approx \alpha_{2}\bar{e}_{2u} + \dot{\bar{e}}_{2u},\tag{31}$$

where $\alpha_2 > 0$ is a positive constant. The control law is designed as:

$$U_2 = u_{2eq} + u_{2s}, (32)$$

Appl. Sci. 2022, 12, 5792 8 of 16

where u_{2eq} is the equivalent control and u_{2s} is the reaching law designed as:

$$u_{2eq} = -\hat{m}\overline{A}_2 - \delta_2, u_{2s} = \dot{s}_2 = -\hat{m}C_{23}^{-1}[K_2s_2 + \eta_2\operatorname{sig}^{\sigma_2}(s_2)],$$
(33)

with

$$\overline{A}_{2} = C_{23}^{-1} \left[(\dot{C}_{22} + \ddot{C}_{21}) e_{2u} + \dot{C}_{23} e_{2a} + (C_{22} + \dot{C}_{21}) (A_{21} e_{2u} + A_{22} e_{2a}) + C_{23} e_{2a} \right]
+ (A_{23} e_{2u} + A_{24} e_{2a}) + \alpha_{2} C_{23}^{-1} \left[(C_{22} + \dot{C}_{21}) e_{2u} + C_{23} e_{2a} \right],$$

$$\delta_{2} = C_{23}^{-1} \left[(C_{22} + \dot{C}_{21}) d_{2u} \right] + d_{2a} + \alpha_{2} C_{23}^{-1} C_{21} d_{2u},$$
(34)

where $K_2 > 0$, $\eta_2 > 0$ are the positive constants. Then the switching control law combining the neural network control law and the adaptive sliding mode control law is designed as:

$$U_2 = -\hat{m}\overline{A}_2 + (1 - \hbar_{a,b}(e_o))u_{n2} + \hbar_{a,b}(e_o)u_{s2} + u_{2s}, \tag{35}$$

with

$$u_{n2} = -\hat{W}_2^{\mathrm{T}} h(X) - \operatorname{diag}(\hat{\phi}_{21}, \hat{\phi}_{22}) \operatorname{sgn}(s_2), u_{s2} = -\hat{\delta}_2.$$
 (36)

The adaptive laws of \hat{m} , \hat{W}_2 , $\hat{\phi}_2$ and $\hat{\delta}_2$ in Equation (35) are designed as:

$$\begin{cases}
\dot{\hat{m}} = \gamma_2 s_2^{\mathrm{T}} \overline{A}_2, \\
\dot{\hat{W}}_2 = (1 - \hbar_{a,b}(\boldsymbol{e}_{\rho})) \boldsymbol{\xi}_1 \boldsymbol{h}(\boldsymbol{X}) \boldsymbol{s}_2^{\mathrm{T}}, \\
\dot{\hat{\boldsymbol{\phi}}}_2 = (1 - \hbar_{a,b}(\boldsymbol{e}_{\rho})) \boldsymbol{\xi}_2 | \boldsymbol{s}_2 |, \\
\dot{\hat{\boldsymbol{\delta}}}_2 = \hbar_{a,b}(\boldsymbol{e}_{\rho}) \boldsymbol{\xi}_3 \boldsymbol{s}_2,
\end{cases} (37)$$

where $\gamma_2 > 0$, ξ_1 , ξ_2 and ξ_3 are positive definite diagonal matrices. Consider the Lyapunov function V_2 designed as:

$$V_2 = (1/2)(s_2^{\mathrm{T}} m s_2 + \gamma_2^{-1} \widetilde{m}^2 + \operatorname{tr}(\widetilde{W}_2^{\mathrm{T}} \xi_1 \widetilde{W}_2) + \widetilde{\boldsymbol{\phi}}_2^{\mathrm{T}} \xi_2^{-1} \widetilde{\boldsymbol{\phi}}_2 + \widetilde{\delta}_2^{\mathrm{T}} \xi_3^{-1} \widetilde{\delta}_2)$$
(38)

where $\widetilde{W}_2 = \hat{W}_2 - W_2^*$, $\widetilde{\phi}_2 = \hat{\phi}_2 - \phi_2$ and $\widetilde{\delta}_2 = \hat{\delta}_2 - \delta_2$ are the estimation errors of W_2^* , ϕ_2 and δ_2 , respectively. Similar to the method used in the stability proof of radial underactuated, the same asymptotic stability of the closed-loop system can be proved for the case without in-track control and will not be repeated.

4. Simulations

The performance of the proposed controllers will be demonstrated by simulating a reconfiguration scenario and comparing the fuel consumption in two underactuated cases. The chief satellite flies in elliptical orbits and the orbital elements for the chief are given in Table 1.

Table 1. Initial orbital elements of the chief spacecraft.

Orbit Element	Value	
Apogee altitude/m	3×10^{6}	
Perigee altitude/m	5×10^5	
Inclination/deg	40	
Right ascension of ascending node/deg	60	
Argument of perigee/deg	270	
True anomaly/deg	0	

The initial mass of the deputy is m = 10 kg, the deputy's estimated mass is $\hat{m} = 8$ kg. The matrix $C \in \mathbb{R}^{12 \times 5}$ in RBFNN is chosen as:

$$C = \left[\frac{\overline{C}_1}{\overline{C}_2} \right], \tag{39}$$

with

$$\overline{C}_{1} = \begin{bmatrix}
-1000 & -500 & 0 & 500 & 1000 \\
-600 & -300 & 0 & 500 & 1000 \\
-1000 & -500 & 0 & 500 & 1000 \\
-0.5 & -0.25 & 0 & 0.25 & 0.5 \\
-1.0 & -0.5 & 0 & 0.5 & 1.0 \\
-1.0 & -0.5 & 0 & 0.5 & 1.0
\end{bmatrix}, \overline{C}_{2} = \begin{bmatrix}
-250 & -125 & 0 & 125 & 250 \\
-600 & -300 & 0 & 500 & 1000 \\
-500 & -250 & 0 & 250 & 500 \\
-0.3 & -0.15 & 0 & 0.15 & 0.3 \\
-0.5 & -0.25 & 0 & 0.25 & 0.5 \\
-0.5 & -0.25 & 0 & 0.25 & 0.5
\end{bmatrix}.$$
(40)

4.1. Case without the Radial Control

The deputy's initial state is $X_I(t_0) = \begin{bmatrix} 0 & 1000 & 0 & 0.5 & 0 & 1 \end{bmatrix}^T$, the terminal state of the deputy is $X_I(t_f) = \begin{bmatrix} 0 & 500 & 0 & 0.3 & 0 & 0.5 \end{bmatrix}^T$, given that J2 perturbation is the main disturbance in LEO. A nonlinear dynamical model of J2-perturbed spacecraft relative motion is introduced to evaluate the robustness of the system [27]. Meanwhile, another periodic disturbance is also incorporated into the dynamical model expressed as:

$$\mathbf{D} = D_m \begin{bmatrix} \sin(n_C t) \\ \sin(n_C t) \\ \cos(n_C t) \end{bmatrix},\tag{41}$$

where D_m is a constant. Furthermore, the linear sliding mode controller (LSMC) was introduced for comparative analysis [10]. For the case without radial thrust, the LSMC is designed as:

$$U_{L1} = -m_0((A_{13}e_{1u} + A_{14}e_{1a}) + P_{12}(A_{11}e_{1u} + A_{12}e_{1a}) + c_1(P_{12}e_{1u} + e_{1a}) + K_{11}s_{L1} + K_{12}sig^{\sigma_1}(s_{L1}))$$
(42)

The sliding mode surface is designed as $s_{L1} = e_{1a} + P_{12}e_{1u} + c_1\tilde{e}_{1u}$, where $c_1 > 0$ is the controller parameter. Furthermore, k_{11} , k_{12} and k_{13} , are selected according to ideas given in [13]. The other control parameters for SNNC and LSMC are shown in Table 2. To facilitate comparison between the two types of controllers, the controller parameters are selected on the principle that similar control energy is consumed to complete the formation reconfiguration mission.

Table 2. Closed-loop controller parameters without radial control.

Controller	Parameter		
	$\alpha_1 = 2 \times 10^{-3}$, $\gamma_1 = 1$, $k_{11} = 0.99\sqrt{2} k_{12} $,		
SNNC	$k_{12} = -1.95\sqrt{\omega_{\text{C}}}, k_{13} = 1/\sqrt{\omega_{\text{C}}}, K_1 = diag(2 \times 10^{-3}, 3 \times 10^{-3}),$		
	$\eta_1 = diag(10^{-5}, 10^{-6}), \xi_1 = diag(8.4 \times 10^{-5}, 8.4 \times 10^{-5}),$		
	$\xi_2 = diag(4 \times 10^{-4}, 8 \times 10^{-6}),$		
	$\xi_3 = diag(1.5 \times 10^{-6}, 1 \times 10^{-7}), a = 6, b = 50, \sigma_1 = 0.5,$		
	$b_i = 1.2 \times 10^3$		
LCMC	$a_1 = 2 \times 10^{-3}$, $k_{11} = 0.99\sqrt{2} k_{12} $, $k_{12} = -1.95\sqrt{\omega_C}$, $k_{13} = 1/\sqrt{\omega_C}$,		
LSMC	$K_{11} = 10^{-3} \cdot diag(2,3), K_{12} = 10^{-6} \cdot diag(10,1), \sigma_1 = 0.5$		

A comparison of the relative position errors and velocity errors of the SNNC and LSMC are shown in Figures 2 and 3. Details of the trajectories of relative position errors and relative velocity errors since T is also enlarged in the right side of Figures 2 and 3, respectively, from which it can be seen that the steady-state relative position error for both

types of controllers is in the order of 10^0 m. The steady-state error is smaller and the control accuracy is higher with the SNNC compared to the LSMC controller.

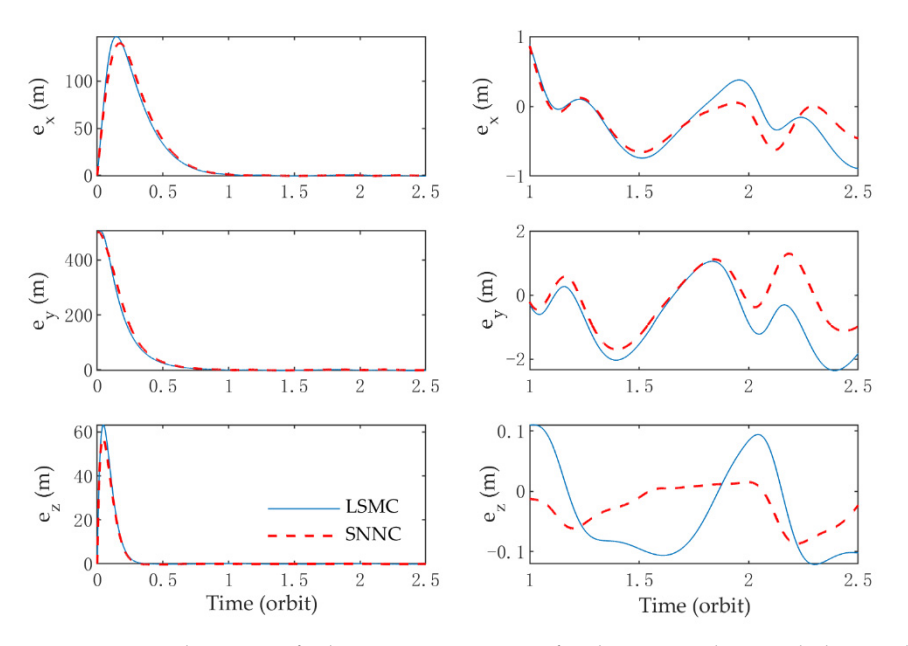


Figure 2. Time histories of relative position errors for the case without radial control.

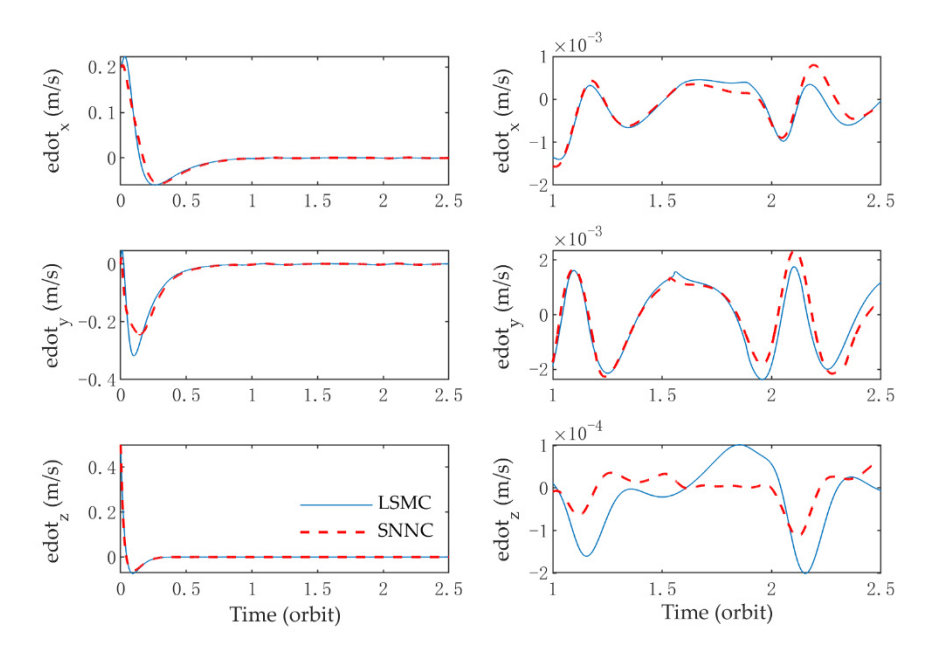


Figure 3. Time histories of relative velocity errors for the case without radial control.

Comparisons of the SNNC and LSMC control input are depicted in Figure 4, with a magnitude of $10^{-3}~\rm m/s^2$ and approximately 0.8 period to reach steady state. The reconfiguration trajectory of the spacecraft is shown in Figure 5, which shows that the SNNC is able to perform the formation reconfiguration mission and verifies the feasibility of formation reconfiguration in the absence of radial thrust.

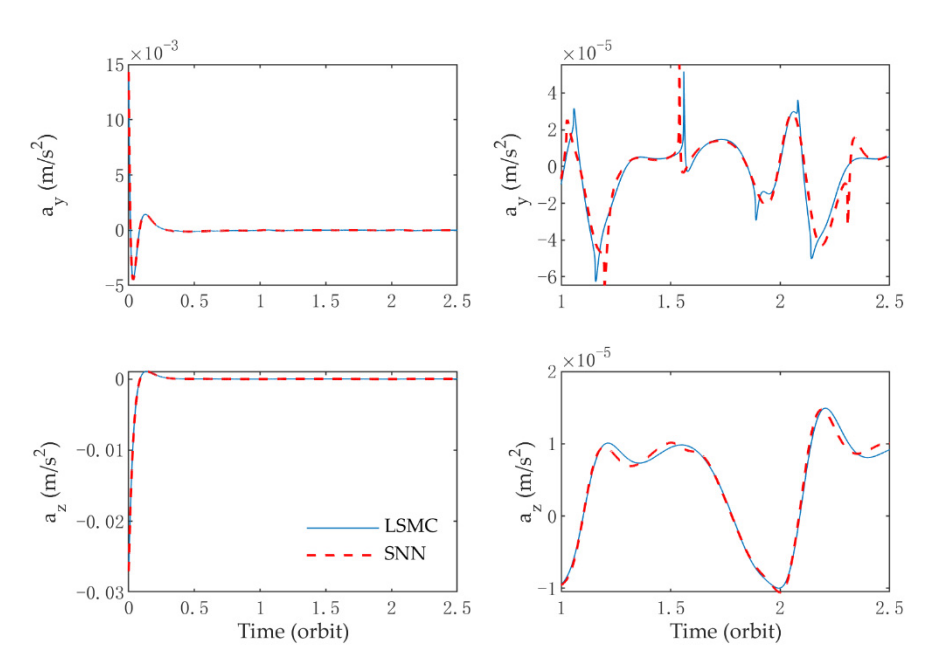


Figure 4. Time histories of control inputs for the case without radial control.

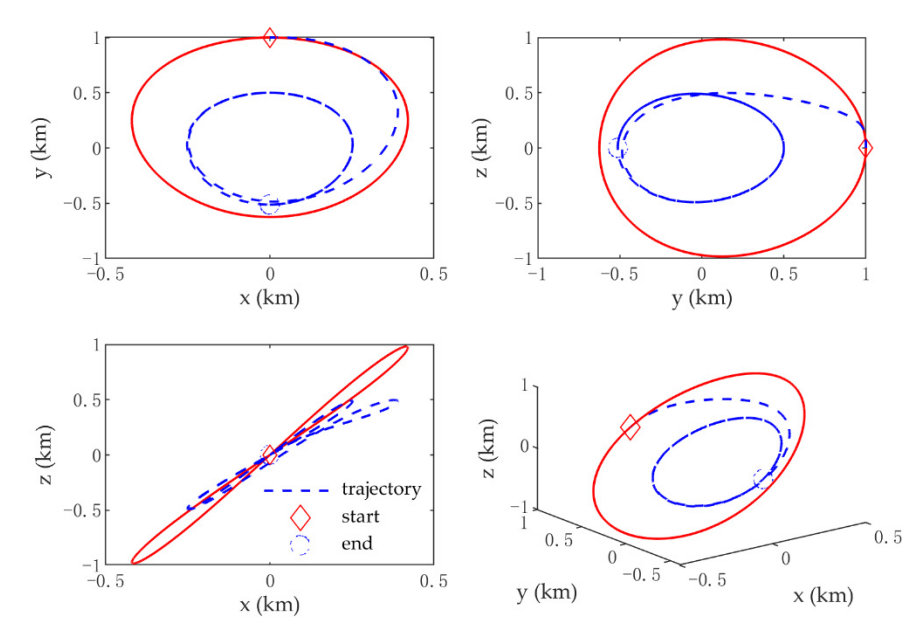


Figure 5. Trajectories of relative transfer orbit and formation for the case without radial control.

To further compare the performance of the two types of controllers, the following evaluation indicators are defined. Denote a = U/m as the control acceleration, then the control energy consumption is defined as $J = \int_{t_0}^{t_f} (a^T a/2) dt$, and the velocity incremental consumption is defined as $\Delta V = \int_{t_0}^{t_f} \|a\| dt$. t_s is the settling time required for the relative distance error $\|e_{\rho}(t)\|$ to converge and remain within 1% of its initial value $\|e_{\rho}(0)\|$, that is $\forall t \geq t_s$, $\|e_{\rho}(t)\| \leq 1\% \|e_{\rho}(0)\|$. The average steady-state relative distance error is defined as

$$d_{s} = \max_{t_{s} \le t \le t_{f}} \{ \| \boldsymbol{e}_{\rho}(t) \| \}. \tag{43}$$

Quantitative comparisons on the performance indices of these two controllers are summarized in Table 3, showing that the SNNC has faster convergence and a 20.7% reduction in steady-state error compared to the LSMC controller for the same amount of control energy consumed, providing higher control accuracy.

- 1 1	_	D (. 1	•
Iabla	~~	Parta	rmance	1100	1000
Iable	J.	I CIIO	шансе	ши	IICCS.

Case	Performance Index			
	t_s , Orbit	d_s , m	ΔV, m/s	J , m^2/s^3
SNNC	0.82	1.03	0.77	4.61×10^{-4}
LSMC	0.82	1.30	0.77	4.61×10^{-4}

4.2. Case without the In-Track Control

For the case without in-track control, the LSMC is designed as

$$U_{L2} = -m_0((A_{23}e_{2u} + A_{24}e_{2a}) + P_{22}(A_{21}\overline{e}_{2u} + A_{22}e_{2a}) + c_2(P_{22}\overline{e}_{2u} + e_{2a}) + K_{21}s_{L2} + K_{22}\operatorname{sig}^{\sigma_2}(s_{L2})). \tag{44}$$

The sliding mode surface is designed as $s_{L2} = e_{2a} + P_{22}\bar{e}_{2u} + c_2\tilde{e}_{2u}$, where $c_2 > 0$ is the controller parameter. The other control parameters for SNNC and LSMC are shown in Table 4. Similar to the case without the radial control, the controller parameters are selected on the principle that similar control energy is consumed to complete the formation reconfiguration mission.

Table 4. Closed-loop controller parameters without in-track control.

Controller	Parameter
SNNC	$\alpha_2 = 1 \times 10^{-3}$, $\gamma_1 = 1$, $k_{21} = -0.25$, $k_{22} = -500$, $K_2 = diag(1 \times 10^{-3}, 3 \times 10^{-3})$, $\eta_2 = diag(1 \times 10^{-6}, 1 \times 10^{-6})$, $\xi_1 = diag(8 \times 10^{-6}, 8 \times 10^{-6})$, $a = 6$, $b = 50$, $\xi_2 = diag(1 \times 10^{-6}, 8 \times 10^{-6})$
LSMC	1×10^{-9}), $\xi_3 = diag(1.3 \times 10^{-9}, 1 \times 10^{-8})$, $b_j = 1.2 \times 10^3$, $\sigma_1 = 0.5$ $a_2 = 2 \times 10^{-3}$, $k_{21} = -0.25$, $k_{22} = -500$, $K_{21} = diag(1 \times 10^{-3}, 3 \times 10^{-3})$, $K_{22} = diag(1 \times 10^{-6}, 1 \times 10^{-6})$, $\sigma_1 = 0.5$

Time histories of the relative position errors and velocity errors of the SNNC and LSMC are shown in Figures 6 and 7, details of the trajectories since T are also enlarged in the right side of Figures 6 and 7, respectively, from which it can be seen that the steady-state relative position error for both types of controllers is in the order of 10^0 m. The steady-state error is smaller and the control accuracy is higher with the SNNC compared to the LSMC controller.

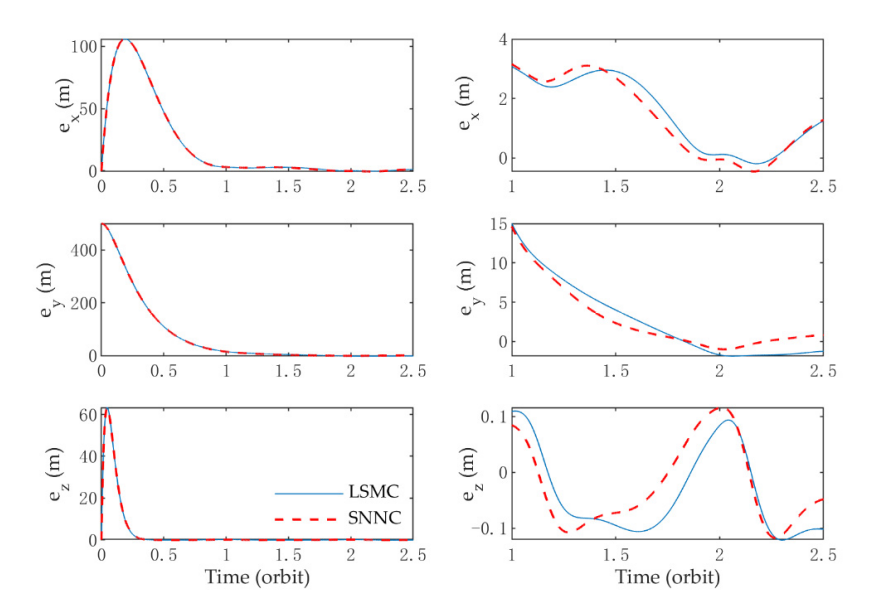


Figure 6. Time histories of relative position errors for the case without in-track control.

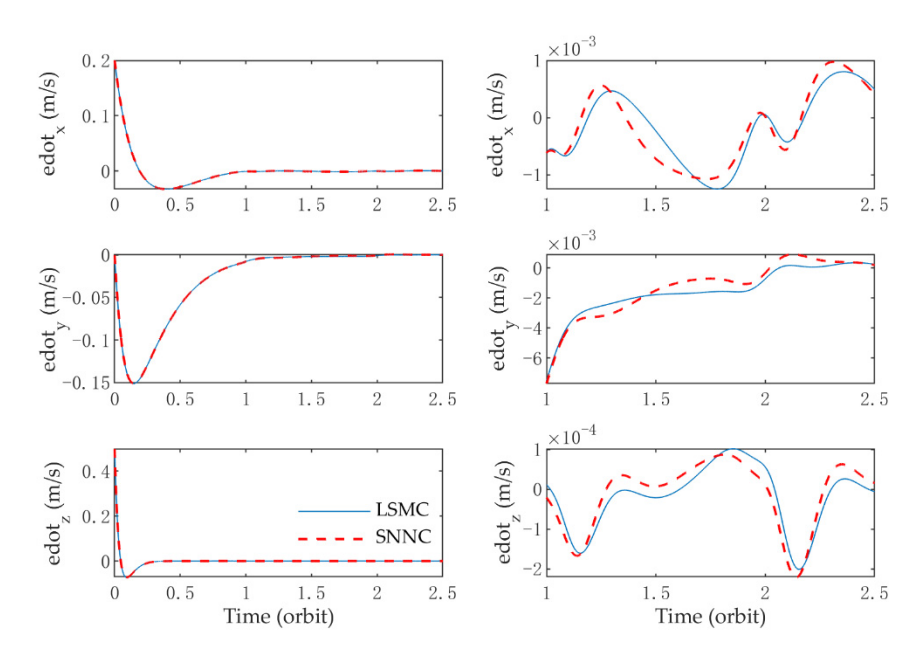


Figure 7. Time histories of relative velocity errors for the case without in-track control.

Figure 8 shows the comparison of the SNNC and LSMC control inputs, with a magnitude of 10^{-3} m/s² and a steady-state time of about 0.8 period. The reconfiguration trajectory of the spacecraft is shown in Figure 9, which shows that the SNNC is capable of managing the formation reconfiguration mission and demonstrating the feasibility of formation reconfiguration with the loss of in-track thrust.

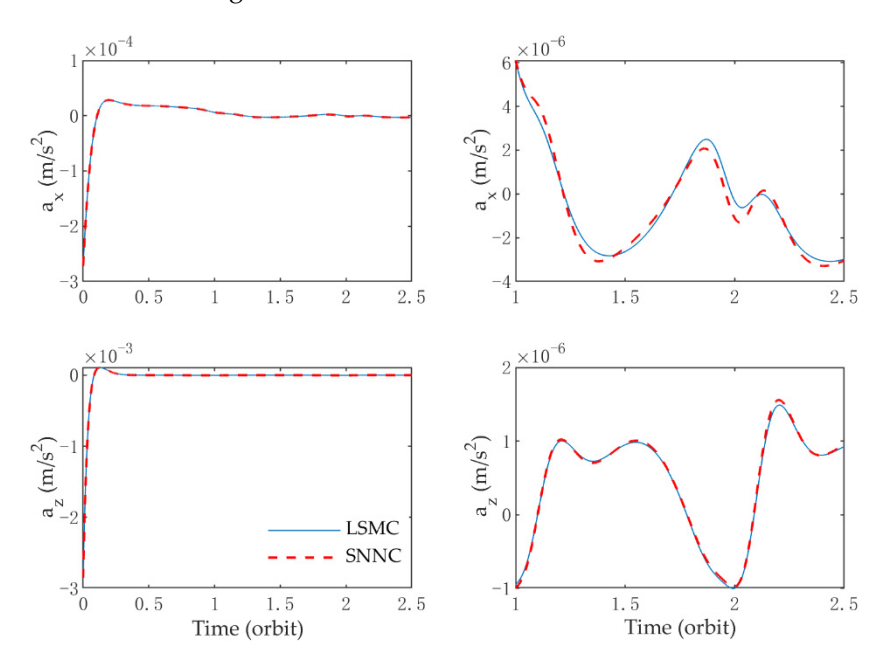


Figure 8. Time histories of control inputs for the case without in-track control.

A comparison of the performance indices for the two controllers is shown in Table 5. Similar to the case with the loss of radial thrust, for the same amount of control energy consumed, the SNNC has faster convergence and a reduction in steady-state error of approximately 33.2% compared to the LSMC controller, providing higher control accuracy.

Appl. Sci. 2022, 12, 5792 14 of 16

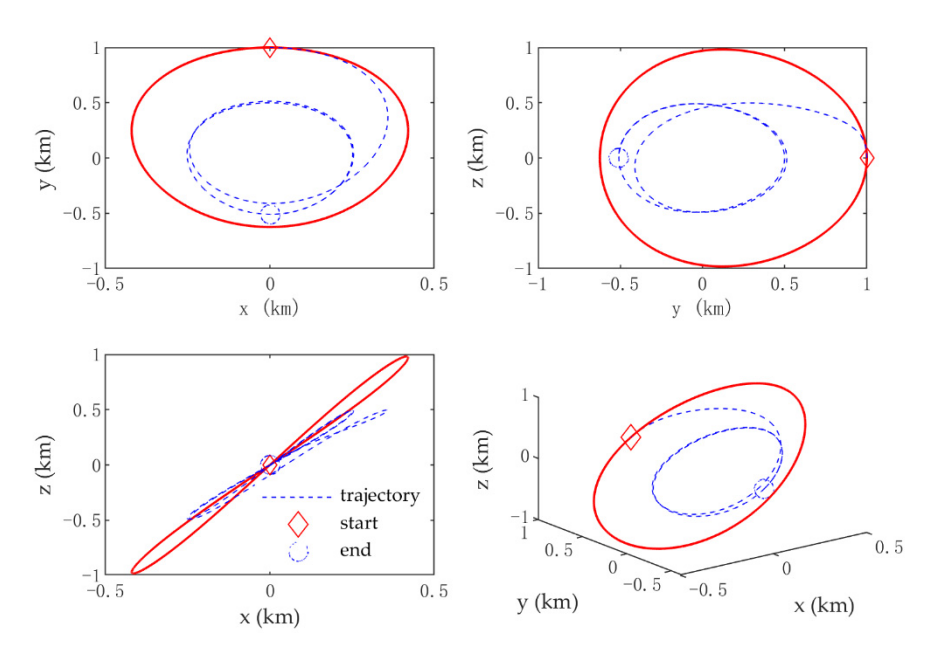


Figure 9. Trajectories of relative transfer orbit and formation for the case without in-track control.

Table 5. Performance indices.

Case	Performance Index			
	t _s , Orbit	d_s , m	ΔV , m/s	J , m^2/s^3
SNNC	1.35	1.45	0.74	4.14×10^{-4}
LSMC	1.46	2.17	0.74	4.14×10^{-4}

5. Conclusions

In this paper, the SNNC for underactuated formation reconfiguration in elliptical orbit is designed. A linear time-varying dynamical model is used to describe the relative motion of the deputy satellite with respect to the chief. To guarantee trajectory tracking in the presence of thrust failures and unmatched disturbance, the SNNC consisting of the adaptive neural network controller and sliding mode controller is proposed. RBFNN is used to approximate the uncertainty term in the dynamical system and an adaptive law derived via the Lyapunov-based method is used to estimate the upper bound on the approximation error, which avoids the requirement for a priori knowledge of the upper bound on the approximation error and ensures the overall stability of the system. The SNNC, combining the adaptive neural network with adaptive sliding mode work cooperatively, not only improves the control accuracy, but also prevents the adverse effects of inaccurate neural network estimation on the system. The simulation results indicate that the proposed SNNC can obtain higher control accuracy than the LSMC and improve disturbance rejection performance, and the proposed controller could be directly applied to a series of formation reconfiguration missions in the near future. Furthermore, the controller can be adopted in other similar relative orbital control problems, such as spacecraft rendezvous and hovering. The current research focuses on formation reconfiguration in elliptical orbits. In future, we plan to extend our current work in two directions. First, we will extend our work to output feedback control schemes for underactuated spacecraft reconfiguration with the loss of velocity measurements and thrust simultaneously. Second, we will extend our work to similar reconfiguration problems in elliptic orbits using relative orbit elements to reduce the tracking error.

Appl. Sci. 2022, 12, 5792 15 of 16

Author Contributions: Z.L. supervised the research and reviewed the manuscript. J.Y. carried out the investigation, methodology, analysis, and wrote the original manuscript. L.J. and Y.Z. carried out the simulations, analyzed the results and checked the structure of the paper. All authors have read and agreed to the published version of the manuscript.

Funding: This research was funded by Young Scientists Fund of the National Natural Science Foundation of China (Grant No: 61906213).

Institutional Review Board Statement: Not applicable.

Informed Consent Statement: Not applicable.

Data Availability Statement: Not applicable.

Conflicts of Interest: The authors declare no conflict of interest.

References

 Lee, D.; Sanyal, A.K.; Butcher, E.A. Asymptotic Tracking Control for Spacecraft Formation Flying with Decentralized Collision Avoidance. J. Guid. Control. Dyn. 2015, 38, 587–600. [CrossRef]

- 2. Chung, S.J.; Bandyopadhyay, S.; Foust, R.; Subramanian, G.P.; Hadaegh, F.Y. Review of Formation Flying and Constellation Missions Using Nanosatellites. *J. Spacecr. Rocket.* **2016**, *53*, 567–578. [CrossRef]
- 3. Delpech, M.; Berges, J.C.; Karlsson, T.; Malbet, F. Results of PRISMA/FFIORD Extended Mission and Applicability to Future Formation Flying and Active Debris Removal Missions. *Int. J. Sp. Sci. Eng.* **2013**, *1*, 382–409. [CrossRef]
- 4. Guibout, V.M.; Scheeres, D.J. Spacecraft Formation Dynamics and Design. J. Guid. Control. Dyn. 2006, 29, 121–133. [CrossRef]
- 5. Huang, X.; Yan, Y.; Zhou, Y. Underactuated Spacecraft Formation Reconfiguration with Collision Avoidance. *Acta Astronaut.* **2017**, 131, 166–181. [CrossRef]
- 6. Park, H.E.; Park, S.Y.; Choi, K.H. Satellite Formation Reconfiguration and Station-Keeping Using State-Dependent Riccati Equation Technique. *Aerosp. Sci. Technol.* **2011**, *15*, 440–452. [CrossRef]
- 7. Zhou, N.; Chen, R.; Xia, Y.; Huang, J.; Wen, G. Neural Network–Based Reconfiguration Control for Spacecraft Formation in Obstacle Environments. *Int. J. Robust Nonlinear Control* **2018**, *28*, 2442–2456. [CrossRef]
- 8. Leonard, C.; Hollister, W.M.; Bergmann, E.V. Orbital formation keeping with differential drag. *J. Guid. Control. Dyn.* **1989**, 12, 108–113. [CrossRef]
- 9. Kumar, K.D.; Bang, H.C.; Tahk, M.J. Satellite formation flying using along-track thrust. *Acta Astronaut*. **2007**, *61*, 553–564. [CrossRef]
- 10. Godard, D.; Kumar, K.; Zou, A. Robust Stationkeeping and Reconfiguration of Underactuated Spacecraft Formations. *Acta Astronaut*. **2014**, *105*, 495–510. [CrossRef]
- 11. Yin, J.; Han, C. Elliptical Formation Control Based on Relative Orbit Elements. Chin. J. Aeronaut. 2013, 26, 1554–1567. [CrossRef]
- 12. Huang, X.; Yan, Y.; Zhou, Y. Analytical Solutions to Optimal Underactuated Spacecraft Formation Reconfiguration. *Adv. Sp. Res.* **2015**, *56*, 2151–2166. [CrossRef]
- 13. Huang, X.; Yan, Y.; Zhou, Y. Dynamics and Control of Underactuated Spacecraft Formation Reconfiguration in Elliptic Orbits. *Proc. Inst. Mech. Eng.* **2018**, 232, 2214–2230. [CrossRef]
- 14. Yoshimura, Y. Optimal Formation Reconfiguration of Satellites under Attitude Constraints Using Only Thrusters. *Aerosp. Sci. Technol.* **2018**, 77, 449–457. [CrossRef]
- 15. Clohessy, W.H.; Wiltshire, R.S. Terminal Guidance System for Satellite Rendezvous. J. Aerosp. Sci. 1960, 27, 653–658. [CrossRef]
- 16. Tschauner, J.; Hempel, P. Rendezvous with a Target in an Elliptical Orbit. Astronaut. Acta 1965, 11, 104–109.
- 17. Li, J.; Xi, X.N. Fuel-Optimal Low-Thrust Reconfiguration of Formation-Flying Satellites via Homotopic Approach. *J. Guid. Control. Dyn.* **2012**, 35, 1709–1717. [CrossRef]
- 18. Palmer, P. Optimal Relocation of Satellites Flying in Near-Circular-Orbit Formations. *J. Guid. Control. Dyn.* **2006**, 29, 519–526. [CrossRef]
- 19. Zou, A.M.; Kumar, K.D.; Hou, Z.G. Quaternion-Based Adaptive Output Feedback Attitude Control of Spacecraft Using Chebyshev Neural Networks. *IEEE Trans. Neural Netw.* **2010**, *21*, 1457–1471.
- 20. Zou, A.M.; Kumar, K.D.; Hou, Z.G.; Liu, X. Finite-Time Attitude Tracking Control for Spacecraft Using Terminal Sliding Mode and Chebyshev Neural Network. *IEEE Trans. Syst. Man Cybern. Part B* **2011**, *41*, 950–963. [CrossRef]
- 21. Zou, A.M.; Kumar, K.D. Adaptive Output Feedback Control of Spacecraft Formation Flying Using Chebyshev Neural Networks. *J. Aerosp. Eng.* **2011**, 24, 361–372. [CrossRef]
- 22. Sun, T.; Pei, H.; Pan, Y.; Zhou, H.; Zhang, C. Neural Network-Based Sliding Mode Adaptive Control for Robot Manipulators. *Neurocomputing* **2011**, *74*, 2377–2384. [CrossRef]
- 23. Xia, K.; Huo, W. Robust Adaptive Backstepping Neural Networks Control for Spacecraft Rendezvous and Docking with Input Saturation. *ISA Trans.* **2016**, *62*, 249–257. [CrossRef]
- 24. Sun, R.; Wang, J.; Zhang, D.; Shao, X. Neural-Network-Based Sliding-Mode Adaptive Control for Spacecraft Formation Using Aerodynamic Forces. *J. Guid. Control. Dyn.* **2018**, *41*, 754–760. [CrossRef]

25. Sun, R.; Wang, J.; Zhang, D.; Shao, X. Neural Network-Based Sliding Mode Control for Atmospheric-Actuated Spacecraft Formation Using Switching Strategy. *Adv. Sp. Res.* **2018**, *61*, 914–926. [CrossRef]

- 26. Wu, J.; Chen, W.; Zhao, D.; Li, J. Globally Stable Direct Adaptive Backstepping NN Control for Uncertain Nonlinear Strict-Feedback Systems. *Neurocomputing* **2013**, 122, 134–147. [CrossRef]
- 27. Xu, G.; Wang, D. Nonlinear Dynamic Equations of Satellite Relative Motion around an Oblate Earth. *J. Guid. Control. Dyn.* **2008**, 31, 1521–1524. [CrossRef]